Numerical Optimization Strategy for Determining 3D Flow Fields in Microfluidics

A. Eden*[1], M. Sigurdson[1], C. D. Meinhart[1], I. Mezić[1]
[1] University of California, Santa Barbara, Department of Mechanical Engineering
*Corresponding author: Department of Mechanical Engineering, University of California, Santa Barbara, Santa Barbara, CA 93106-5070. Email: a_eden@umail.ucsb.edu

Abstract: Measurement of three dimensional, three component velocity fields is central to the development of effective micromixers for bioassays and lab-on-chip mixing applications. We present a hybrid experimental-numerical method for the generation of 3D flow information from 2D particle image velocimetry (PIV) experimental data and finite element simulations. An optimization algorithm is applied to a theory-based simulation of an alternating current electrothermal (ACET) micromixer in conjunction with 2D PIV data to generate an improved estimation of the 3D steady state flow conditions. This 3D data can be used to assess the flow conditions and mixing phenomena of such devices more accurately than would be possible through simulation alone. The optimization algorithm reduced the normalized root mean square error (NRMSE) between the experimental and simulated velocity fields in the target region by more than an order of magnitude.

Keywords: microfluidics, electrothermal flow, optimization, PIV

1. Introduction

Electrokinetic flows produced by alternating current (AC) electric fields have been studied extensively and have proven to be an effective means of driving fluids and particles in applications such as mixing, stirring, and pumping [1-4]. These AC electrokinetic phenomena can be broadly classified into the categories of electrothermal effects, electroosmosis, and dielectrophoresis (DEP) [2]. Fluid motion from electrothermal effects is due to the interaction of an electric field with thermally induced conductivity and permittivity gradients within the fluid. AC electroosmosis occurs when the tangential component of an electric field interacts with a field-induced electric double layer around a solid surface, resulting in a net body force on the fluid. Dielectrophoretic forces act on particles and result from differences in polarizability between a particle and fluid medium in the presence of a non-uniform electric field [3]. Here we study externally induced thermal gradients from Joule heating, resulting in fluid circulation due to electrothermal and buoyancy forces. Dielectrophoretic forces on tracer particles are also calculated and included to account for any DEP effects, which are most significant for particles near the electrodes. The frequencies on the order of 1 MHz in our experiments are much larger than typical electrode polarization frequencies; AC electroosmotic effects are negligible because the charge has insufficient time to accumulate in the diffuse double layer [5]. In our micromixer, configurable electrothermal fluid motion is generated by applying distinct AC signals to each of 5 different electrodes. These voltage patterns can include different signal phases and be periodically switched to induce chaotic mixing, but here we study the steady state case [4].

Current methods for generating 3D velocity fields from PIV experiments require multiple-camera setups and processing software. These 3D PIV methods can be challenging to implement and can result in lower quality data than certain 2D methods. A 3D POD PIV algorithm developed by Kauffman *et al* [6] for generating out-of-plane velocity components from successive 2D measurements would require 16 interrogation regions to span the entire mixing chamber, each requiring measurements at 20 different height levels. Such large, data-intensive experiments can introduce problems such as drift from various sources, as well as error from stitching the data together.

Numerical simulation models of ACET flow have been developed using finite element packages such as *COMSOL Multiphysics*. For this micromixer, a combination of built-in physics simulation modules and manually programmed partial differential equations were used to numerically represent the governing

physical equations and recreate the PIV experimental conditions through simulation, following Loire *et al* [7]. However, these simulations often have significant discrepancies with measurements for a variety of reasons including inhomogeneous material properties, inexact experimental geometries, and assumptions made to simplify physical models. To refine this technique and develop a more accurate physical representation of the experiment, we introduce an optimization algorithm that inputs a velocity field obtained through 2D PIV experiments and minimizes the velocity error between the experimental data and the simulation results at the measurement plane. This method allows us to generate more accurate out-of-plane information in the simulation by scaling physical properties, measurement uncertainty parameters, and the dominant forces involved.

2. Experimental Method

The ACET micromixer we have developed (Figures 1-3) is driven by patterned gold electrodes on an FR4 printed circuit board base. A 450 µm deep, 3 mm x 3 mm PDMS well with a 1 mm thick glass cover defines the mixing chamber. The PIV experiments were conducted with a solution of 0.1X phosphate-buffered saline (PBS) (σ = 1.6 mS/cm) seeded with d_p = 1 µm fluorescent latex beads used as tracer particles. This device was mounted on a copper plate for thermal stasis. A DC power supply and function generator were used to supply a sinusoidal AC signal with an amplified peak-to-peak voltage of V_{pp} = 26 V and a frequency of f = 1 MHz to drive the flow. At this voltage and size scale of tracer particles, Brownian motion is negligible compared to motion from other forces involved [8].

The PIV measurements were made using a µPIV procedure pioneered by Santiago *et al* [9]. The flow field was imaged through an epi-fluorescent microscope (Nikon Eclipse FN1) with a 10X objective lens (Nikon Plan Fluor: NA = 0.30). The focal plane was illuminated with frequency doubled Nd:YAG pulsed lasers (New Wave Research MiniLase II-30), which were controlled by a synchronizer (TSI LaserPulse Synchronizer). Measurements were made at two heights of h_{z_m}= 96 µm and 148 µm above the chamber bottom, with an estimated measurement depth of δ_{z_m}= ±10.75 µm from the focal plane [10]. For each experiment, 100 image pairs (Δt = 10 ms) were recorded by a digital CCD camera (TSI PIVCAM 14-10 cross/auto correlation digital CCD Camera).

The resulting images were of 1376 x 1024 pixel resolution with a square pixel size of 0.64 µm/pixel. These images were processed using software with a custom PIV cross-correlation algorithm that ensemble averages the images and fits a 9-point Gaussian function to the data to determine the particle-image displacement peaks, yielding a 2-dimensional 33 x 24 velocity field for the images taken at each measurement plane [11]. Further data processing was performed on the velocity fields using *CleanVec* vector cleanup software to remove erroneous measurement components. The resulting velocity fields for each interrogation region show a window of data 800 µm x 575 µm in size. Fluid velocities ranging from 1 to 590 µm/s were measured in the various interrogation regions.

While the PIV reproducibly captured the in-plane flow components, the micromixer flow contains significant out-of-plane velocity measurements which could not be measured directly using the current 2D PIV technique. For example, in the central interrogation region (Figures 2 and 3) there are clear regions in the center, top left corner, and bottom right corner with very low in-plane velocities. In these regions, there is significant out-of-plane fluid motion where a combination of buoyancy and electrothermal forces due to localized joule heating drives the flow in vortex patterns up away from the positive electrodes and down towards the negative electrodes. Figure 2 depicts a diagram of the experimental setup.

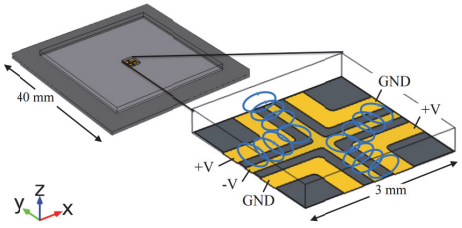

Figure 1: An overview of the ACET micromixer device, depicting the voltage pattern applied to the electrodes during experiments. The general flow pattern is indicated by vertical vortices in between positive and negative electrodes.

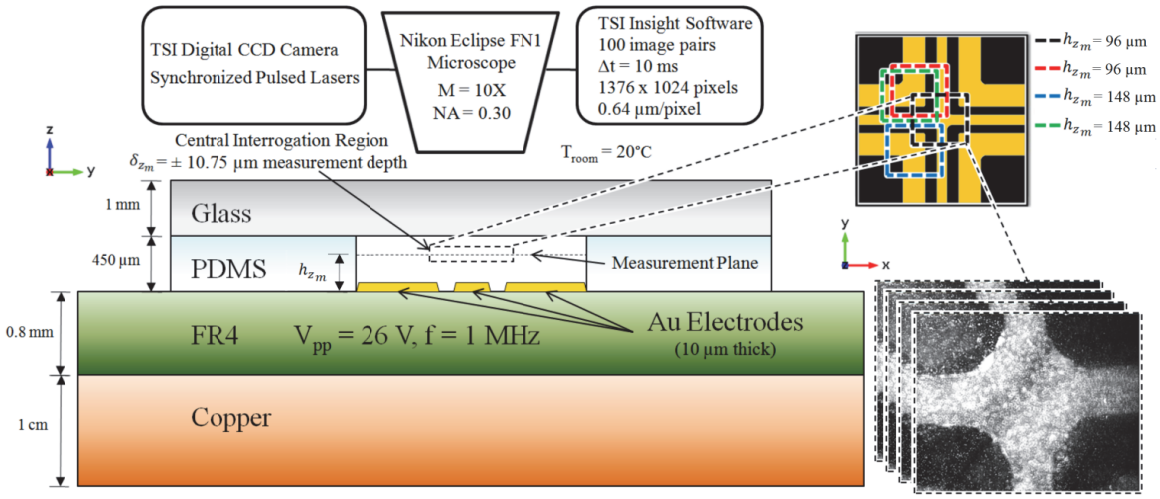

Figure 2: The experimental setup for the 2D PIV flow measurements, portraying a side view of the device and a top view of the electrode design with the voltage pattern used in the experiments and simulations. The four different interrogation region locations are represented by red, blue, black, and green dashed rectangles; images of the central interrogation region captured during a PIV experiment are shown. Note that the diagram is not to scale.

3. Numerical Model

The numerical simulations were performed using *COMSOL Multiphysics* version 5.1 finite element simulation software to solve the temperature and velocity fields as well as the quasi-static electric field. A 3D component matching the design specifications of the device was first created using the *COMSOL Multiphysics* geometry kernel and materials were assigned to specific domains based on the diagram in Figure 2. The simulated physical equations were based on the theoretical model for ac electrokinetic flows developed by Ramos *et al* in [12] and improved by Loire *et al* in [7]. The full enhanced model from [7] presents a simplified and coupled temperature-dependent set of equations, for use in situations where the maximum temperature rise is greater than $\Delta T \approx$ 5°C, which are derived from Gauss's Law and charge conservation, the Joule heating equation, and the Stokes equations. The Joule heating equation and the Stokes equations were solved using the built-in COMSOL physics modules of "heat transfer in fluids" and "laminar single-phase flow", respectively. The boundary conditions for the external surfaces of the modeled device were set to convective heat transfer fluxes with a room temperature of $T_{room} = 20°C$, while the boundary conditions for the solid interior surfaces of the mixing chamber were set to a no-slip condition where $\boldsymbol{u} = 0$. The temperature-dependent form of the electrical convection-diffusion equation was manually entered and solved using the "coefficient form PDE" module, with applied voltage boundary conditions on the electrodes and zero flux boundary conditions on the interior walls of the mixing chamber (i.e. $\frac{\partial V}{\partial n} = 0$). These governing equations from [7] are presented below in (1),

$$\begin{cases} \nabla^2 \tilde{V} = c_\sigma \nabla T \cdot \nabla \tilde{V}, \qquad \tilde{\boldsymbol{E}} = -\nabla \tilde{V} \\ \rho(T) C_p(T) \boldsymbol{u} \cdot \nabla T = \nabla \cdot (k_m \nabla T) + \frac{\sigma_m(T)}{2} |\tilde{\boldsymbol{E}}|^2 \\ \nabla \cdot \left(\mu_m(T)(\nabla \boldsymbol{u} + (\nabla \boldsymbol{u})^T)\right) + \boldsymbol{F} = \nabla P, \qquad \nabla \cdot \boldsymbol{u} = 0 \end{cases} \tag{1}$$

where $\tilde{\boldsymbol{E}}$ is the complex electric field vector, $\tilde{V}$ is the complex potential difference, T is temperature, $\boldsymbol{u}$ is velocity vector, $\rho(T)$, $C_p(T)$, $\sigma_m(T)$, $\mu_m(T)$, k_m are material properties, and c_σ is a constant used in the calculation of the temperature-dependent electrical conductivity. For experiments involving most ACET devices, including those described here, only the real part of the electric field and potential are nonzero due to a phase difference of 0 or $\pi/2$ between electrodes [7]. Empirically-based temperature-dependent functions from COMSOL were used for the fluid density, specific heat, and viscosity to evaluate these properties in the simulation.

The electrical conductivity and permittivity of the aqueous fluid medium were approximated as linear, temperature-dependent equations described by $\sigma_m = \sigma_m(T_0)\big(1 + c_\sigma(T - T_0)\big)$ and $\varepsilon_m = \varepsilon_m(T_0)\big(1 + c_\varepsilon(T - T_0)\big)$, respectively, where $c_\sigma = \frac{1}{\sigma_m(T_0)}\left(\frac{\partial \sigma_m}{\partial T}\right)\Big|_{T_0} \approx 0.02\ ^\circ\mathrm{C}^{-1}$, $c_\varepsilon = \frac{1}{\varepsilon_m(T_0)}\left(\frac{\partial \varepsilon_m}{\partial T}\right)\Big|_{T_0} \approx -0.004\ ^\circ\mathrm{C}^{-1}$, and T_0 is a reference temperature [13]. The parameter c_σ is used in (1) instead of c_ε because the charge relaxation time for our experiments, given by $\tau = \frac{\varepsilon_m(T_0)}{\sigma_m(T_0)}$, is much less than the period of the applied AC signal [7].

The net external body forces include the time-averaged electrothermal force, the buoyancy force, and the dielectrophoretic force**.** The force $\boldsymbol{F}$ solved for in the Stokes equations consists only of the electrothermal force and the buoyancy body forces, the equations for which are shown in (2); since the dielectrophoretic force acts on polarizable particles, this term was not used directly in the solution of the Stokes equations. Instead, the dielectrophoretic velocity was calculated independently with (3) and used to correct the numerically solved velocity field to account for the presence of DEP forces on tracer particles [14]. The dielectrophoretic force is proportional to the cube of the particle radius, the permittivity of the fluid medium, the gradient of the squared RMS electric field, and the real part of the complex term in (3), which is the Clausius-Mossotti Factor. This term accounts for the frequency dependence of the complex permittivities of the fluid medium and the tracer particles due to field-induced dipoles. The complex permittivity equations for the particle and fluid medium are given by $\varepsilon_p{}^* = \varepsilon_p - j\frac{\sigma_p}{\omega}$ and $\varepsilon_f{}^* = \varepsilon_f - j\frac{\sigma_f}{\omega}$ [14].

$$\begin{cases} \boldsymbol{F} = \boldsymbol{F_{ET}} + \boldsymbol{F_B} \\ \boldsymbol{F_{ET}} = \frac{\varepsilon_m(T)}{2}\left[(c_\varepsilon - c_\sigma)(\nabla T \cdot \tilde{\boldsymbol{E}})\tilde{\boldsymbol{E}} - \frac{1}{2}c_\varepsilon \nabla T|\tilde{\boldsymbol{E}}|^2\right] \\ \boldsymbol{F_B} = \rho(T)\boldsymbol{g} \end{cases} \quad (2)$$

$$\begin{cases} \boldsymbol{F_{DEP}} = 2\pi\varepsilon_m {r_p}^3\left[Re\left(\frac{\varepsilon_p{}^* - \varepsilon_f{}^*}{\varepsilon_p{}^* + 2\varepsilon_f{}^*}\right)\nabla|\tilde{\boldsymbol{E}}|^2\right] \\ \boldsymbol{U_{DEP}} = \frac{\boldsymbol{F_{DEP}}}{6\pi r_p \mu_m(T)} \end{cases} \quad (3)$$

To recreate the experimental conditions more accurately in the simulation and achieve better results, a Gaussian window function centered at the measurement plane was used to account for the measurement depth and focus of the camera and microscope. The velocity of the fluid at each point was multiplied by the Gaussian window function, which decreased rapidly in value with vertical distance away from the measurement plane to represent the out-of-focus particles. The resulting velocity field was then linearly projected onto the measurement plane to simulate the projection of an image taken by a camera. Both the width and location of these Gaussian functions were used as control parameters for the optimization algorithm to account for any uncertainty in the measurement depth and focal plane location.

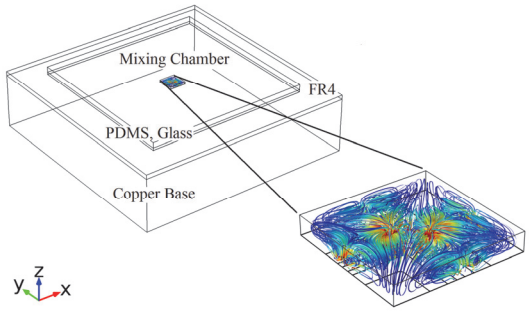

Figure 3: The modeled ACET mixing device with a wireframe rendering and theoretical 3D streamlines for the optimized flow conditions.

3.1 Optimization

The optimization algorithm in the numerical model calculated the mean square error between the PIV velocity measurements and numerically simulated velocity field at each point in the measurement plane, and normalized the resulting values by the velocity magnitude of the PIV measurements. These values, which represent the square of the normalized RMS velocity error, were used as the objective function for minimization**.** The gradient-free Nelder-Mead optimization algorithm was chosen to allow for the use of geometric control parameters that require the re-meshing between successive iterations. The equation for the objective function is shown below in (4).

$$Objective = \frac{\sum (u_{PIV} - u_{Model})^2 + (v_{PIV} - v_{Model})^2}{\sum (u_{PIV})^2 + (v_{PIV})^2} \quad (4)$$

In addition to the location and width of the Gaussian window function, the optimization control parameters included linear scaling factors for the electrothermal, buoyancy, and dielectrophoretic forces (ae, ab, adep) as well as scaling factors for parameters that are not well documented, such as relevant properties of the aqueous PBS solution ($\sigma_m(T_0)$, $\mu_m(T_0)$, k_m) and the anisotropic thermal conductivities of the FR4 printed circuit board (akfr4xx, akfr4yy, akfr4zz). Since our goal is to generate 3D flow measurements for a specific experiment and not to create a predictive model for situations without experimental data, these material properties are not expected to necessarily be scaled to match their true values, but rather are used as handles to shape the flow to match experimental results. The geometrical parameters chosen for optimization include scaling factors for the center electrode widths and the gap between adjacent electrodes (aew, aeg). A voltage scaling factor was also introduced to account for the difference between the nominally applied voltage and measured voltage applied to the electrodes. Objective functions from four different interrogation regions, two at a height of 96 µm and two at a height of 148 µm, were added together for optimization to ensure conditions from throughout the mixer were represented in the final solution.

4. Results and Discussion

Measurement plane velocity fields for the central interrogation region for the µPIV data, original simulation, and optimized simulation are shown in Figure 4. The optimized results match the scale and flow direction of the experimental data. The optimized velocity field has top left and bottom right corner regions of low velocity and flow direction reversal that were not present in the original simulation results; these regions have low in-plane velocities because they represent vertical circulation in the fluid. The optimization changed the general flow pattern at the measurement plane from the original simulation, correcting the excessively large magnitude in the center depicted in Figure 4 as well as removing several horizontal in-plane vortices that developed above the electrodes. The low in-plane velocity in the optimized results shows that the fluid flow between positive and negative electrodes is mostly vertical, indicating the presence of strong buoyancy and electrothermal forces in these regions due to localized joule heating of the electrodes.

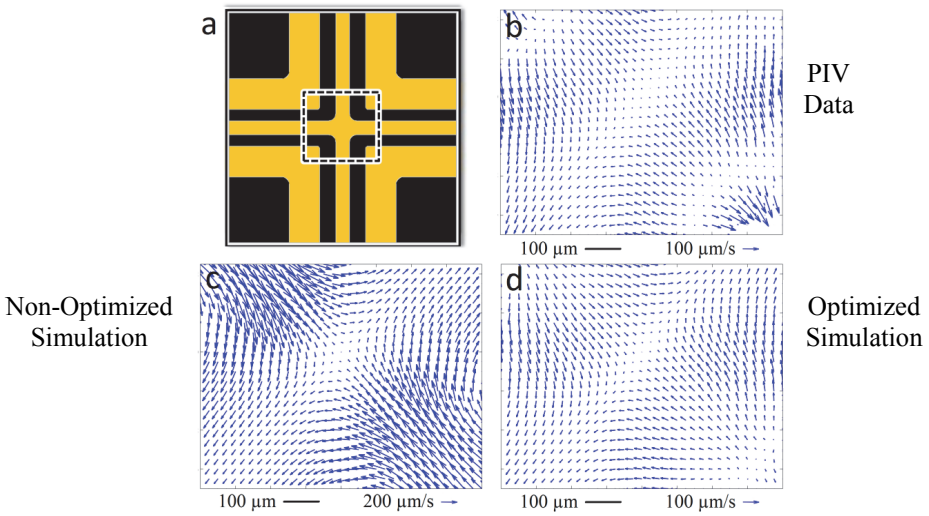

Figure 4: (a) The electrode pattern with an overlay of the central interrogation region location, (b) a top view of the PIV data from the central interrogation region, (c) COMSOL simulation results of the 2D velocity field at the measurement plane for the original estimation of parameters, and (d) optimized COMSOL 2D velocity field at the measurement plane. The simulated and optimized velocity field in (d) depicts regions of reversed flow in the top left and bottom right corners that are present in the PIV measurements but not in the original simulation; however, the locations of these points are slightly offset in the optimized results. The optimized solution also has a much closer velocity magnitude to the results in (b).

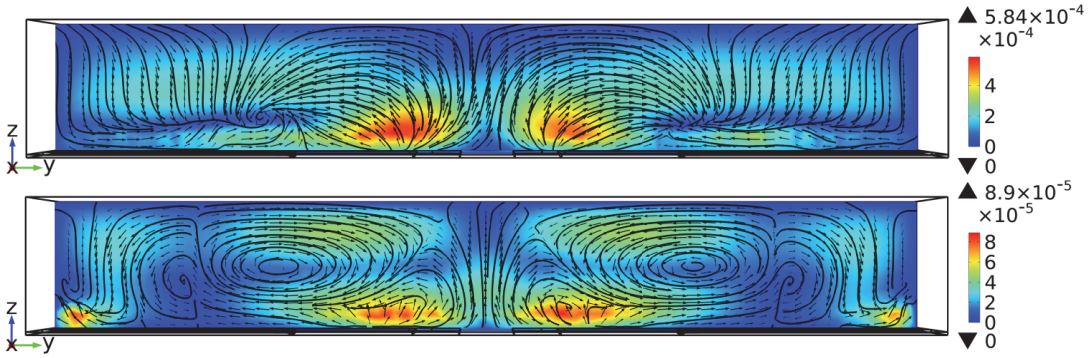

Figure 5: 2D projected velocity fields from a side view of the micromixer for the non-optimized (top) and optimized (bottom) simulation results, in m/s. These velocity fields also depict a complete change in the flow circulation pattern in certain regions from the non-optimized results to the optimized results, visible in the flow direction change everywhere except in the center. Several vertical vortices have developed in the optimized results, representing the flow reversal regions depicted in Figure 4. The maximum velocity magnitude in this plane has been reduced by a factor of roughly 6.5 through optimization.

Figure 5 shows a side view of the velocity field results for a vertical plane in the middle of the mixing chamber. The colored surface plot shows the velocity magnitude, while the vector arrows show the projected velocity direction in this plane. According to the plots, the maximum velocity magnitude in this plane was reduced by a factor of 6.56 through optimization and the direction of the fluid flow changed drastically everywhere except in the center of the device, resulting in circulation patterns within this central plane that are clearly more vertical. In addition to 2D out-of-plane information, we can obtain smooth 3D velocity field information such as the 3D streamlines shown in Figure 3. This information, along with the 2D velocity field results, provides enough information to estimate the general 3D flow patterns of the device under experimental conditions. The numerical 3D velocity, temperature, and electric field data can also be exported for further computational analysis of these mixing devices.

The original and optimized control parameters are shown in Table 1. A comparison of the original and optimized parameters shows how the relevant forces were scaled to match experimental flow conditions, as well as how the geometry and image measurement parameters were slightly altered to achieve a better fit between experimental and numerical results; the optimized width of 20 µm for the Gaussian measurement depth function was close to the theoretical measurement depth of 21.5 µm for the objective lens and fluorescence method used [10]. Scaling of the PBS solution material properties, some of which are sensitive to exact composition and can thus vary considerably, shows that optimization scaled the thermal conductivity, electrical conductivity, and dynamic viscosity by factors of roughly 6, 2, and 1.2, respectively, to better match experimental data. The initial estimates for the anisotropic thermal conductivity components of the FR4 printed circuit board also proved to be considerably lower than the values which ultimately provided a better fit to experimental flow conditions in our model. The initial and optimized parameters are presented in Table 1.

Table 1: Original and optimized values of the chosen physical parameters.

Parameter	Original	Optimized
Electrothermal Force Scaling	1	0.348
Electric Field Nonlinearity Scaling	1	3.125
Buoyancy Force Scaling	1	4.369
Dielectrophoretic Force Scaling	1	3.539
Fluid Thermal Conductivity	0.61 W $m^{-1}K^{-1}$	0.104 W $m^{-1}K^{-1}$
Fluid Electrical Conductivity	1.6 mS/cm	0.84 mS/cm
Fluid Dynamic Viscosity	$9x10^{-4}$ Pa s	$1.12x10^{-3}$ Pa s
Gaussian Function Width	5 µm	20 µm
Measurement Plane Location Offset	0	-48.25 µm
Center Electrode Width	200 µm	160 µm
Gap Width Between Electrodes	200 µm	205 µm
FR4 Thermal Conductivity, x-direction	0.8 W $m^{-1}K^{-1}$	4.25 W $m^{-1}K^{-1}$
FR4 Thermal Conductivity, y-direction	0.8 W $m^{-1}K^{-1}$	3.26 W $m^{-1}K^{-1}$
FR4 Thermal Conductivity, z-direction	0.3 W $m^{-1}K^{-1}$	0.965 W $m^{-1}K^{-1}$

The objective function was reduced by more than a factor of 252 through optimization, resulting in more than an order of magnitude reduction in the normalized RMS velocity error. The NRMSE values between the simulation results and PIV

measurements for the central interrogation region pre- and post- optimization were 2.62 and 0.166, respectively, where NRMSE = $Objective^{1/2}$. These results indicate that the relative error, or the velocity error divided by the PIV velocity magnitude, for the optimized results is only 0.166; that is, the optimized velocity RMS error is less than 17% of the PIV velocity magnitude, compared to an RMS error more than 260% of the velocity magnitude for the non-optimized solution. Results from other interrogation regions showed similar reductions in error, indicating that the remaining regions of the velocity field at the measurement plane are also an improved fit with the experimental results due to continuity and the symmetry of the applied voltage pattern.

5. Conclusion

In this paper, we introduced a hybrid experimental-numerical optimization technique for estimating 3D flow patterns from 2D experimental PIV data. The use of this hybrid optimization method resulted in greater than an order of magnitude reduction in the normalized RMS velocity error between the simulation and 2D PIV experimental results. The optimization algorithm altered 3D fluid circulation patterns considerably, creating a more accurate estimation of the experimental flow field through the scaling of several control parameters. This method shows promise in developing simulations that can more accurately reflect experimental conditions, and has potential applications in modeling flow measurement systems where the dominant physical effects are well characterized and understood.

6. Acknowledgements

Research was supported in part by the Institute for Collaborative Biotechnologies through grant W911NF-09-0001 from the U.S. Army Research Office. The content of the information does not necessarily reflect the position or the policy of the Government, and no official endorsement should be inferred.

7. References

1. A. Gonzáles, A. Ramos, H. Morgan, N.G. Green, A. Castellanos, Electrothermal flows generated by alternating and rotating electric fields in Microsystems, *J. Fluid Mech.* **654** 415-33 (2006)

2. M. Sigurdson, D. Wang, C.D. Meinhart, Electrothermal stirring for heterogeneous immunoassays, *Lab on Chip*, **5**, 1366-73 (2005)

3. M. Sigurdson, D.E. Chang, I. Tuval, I Mezić, C.D. Meinhart, *BioMEMS and Biomedical Nanotechnology*, 243-55, Springer, New York (2007)

4. A. Ramos, H. Morgan, N.G. Green, A. Castellanos, AC Electric-Field-Induced Fluid Flow in Microelectrodes, *Journal of Colloid and Interface Science*, **217(2)**, 420-22 (1999)

5. N.G. Green, A. Ramos, A. González, A. Castellanos, H. Morgan, Electrothermally induced fluid flow in microelectrodes, *Journal of Electrostatics*, **53**, 71-87 (2001)

6. P. Kauffman, S. Loire, I Mezić, C.D. Meinhart, Proper Orthogonal Decomposition based 3D microPIV: application to electrothermal flow study, 10th International Symposium on Particle Image Velocimetry, Delft, The Netherlands, July 1-3, 2013

7. S. Loire, P. Kauffman, I Mezić, C.D. Meinhart, Ac electrokinetics: A theoretical and experimental study of ac electrothermal flows, *J. Phys. D: Appl. Phys*, **45**, 185301 (2012)

8. A. Castellanos, A. Ramos, A. González, N.G. Green, H. Morgan, Electrohydrodynamics and Dielectrophoresis: scaling laws, *J. Phys. D: Appl. Phys*, **36**, 2584-97 (2003)

9. J.G. Santiago, S.T. Wereley, C.D. Meinhart, D.J. Beebe, R.J. Adrian, A particle image velocimetry system for microfluidics, *Exp. Fluids*, **25**, 316-19 (1998)

10. C.D. Meinhart, S.T. Wereley, H.M.B. Gray, Volume illumination for two-dimensional particle image velocimetry, *Measurement Science Technology*, **11**, 809-14 (2000)

11. C.D. Meinhart, S.T. Wereley, J.G. Santiago, A PIV algorithm for estimating time-averaged velocity fields, *J. Fluid Eng.*, **122**, 285-9 (2000)

12. A. Ramos, H. Morgan, N.G. Green, A. Castellanos, Ac electrokinetics: A review of forces in microelectrodes, *J. Phys. D: Appl. Phys.*, **31**, 2338-53 (1998)

13. D.R. Lide, *Handbook of Chemistry and Physics*, CRC Press, New York (2000)

14. M. Liang, Microfluidic manipulation by AC Electrothermal effect, Ph.D diss., University of Tennessee (2010)